nature geoscience

Article

https://doi.org/10.1038/s41561-025-01669-5

Higher precipitation in East Asia and western United States expected with future Southern Ocean warming

Received: 12 April 2024

Accepted: 26 February 2025

Published online: 2 April 2025

Check for updates

Hanjun Kim [1] ✉, Sarah M. Kang [2] ✉, Angeline G. Pendergrass [1,3], Flavio Lehner [1,3,4], Yechul Shin [5], Paulo Ceppi [6], Sang-Wook Yeh [7] & Se-Yong Song [8]

Precipitation over East Asia and the western United States is projected to increase as a result of global warming, although substantial uncertainties persist regarding the magnitude. A key factor driving these uncertainties is the tropical surface warming pattern, yet the mechanisms behind both this warming pattern and the resulting regional precipitation changes remain elusive. Here we use a set of climate model experiments to argue that these changes are partly driven by global teleconnection from the Southern Ocean, which rapidly absorbs anthropogenic heat but releases it with a delay of decades to a century. We show that the delayed Southern Ocean warming contributes to broad tropical ocean warming with an El Niño-like pattern, enhancing precipitation during summer in East Asia and winter in the western United States. The atmospheric teleconnections from the tropical ocean link the Southern Ocean warming to the Northern Hemisphere regional wetting. Southern Hemisphere low clouds are a key regulator of this teleconnection, partly explaining the projected uncertainty of regional precipitation. The documented teleconnection has practical implications: even if climate mitigation reduces carbon dioxide levels, the delayed Southern Ocean warming will sustain a wetter East Asia and western United States for decades to centuries.

Effective adaptation to climate change hinges on accurate regional precipitation projections. This is particularly true for East Asia and the western United States—highly populated regions that experience substantial precipitation variability and associated socioeconomic impacts from flood and droughts[1–3]. State-of-the-art climate models, however, show a high uncertainty of future precipitation changes in these regions[4]. A factor contributing to this uncertainty is inter-model differences in sea surface temperature (SST) projections over the tropics[5–9]. For example, climate models projecting a stronger El Niño-like warming pattern—stronger warming in the eastern equatorial Pacific compared to the western part—tend to exhibit a more pronounced precipitation increase in summer over East Asia[10] and winter over the western United States[11].

However, the underlying drivers of projection uncertainty in tropical SSTs, and thus regional precipitation, remain elusive. A key insight emerges from the common slow timescale shared by the tropical Pacific

[1]Department of Earth and Atmospheric Sciences, Cornell University, Ithaca, NY, USA. [2]Max Planck Institute for Meteorology, Hamburg, Germany. [3]Climate and Global Dynamics Laboratory, National Center for Atmospheric Research, Boulder, CO, USA. [4]Polar Bears International, Bozeman, MT, USA. [5]School of Earth and Environmental Sciences, Seoul National University, Seoul, South Korea. [6]Department of Physics, Imperial College London, London, UK. [7]Department of Marine Science and Convergence Engineering, Hanyang University, ERICA, Ansan, South Korea. [8]Earth Research Institute, University of California, Santa Barbara, CA, USA. ✉e-mail: hk764@cornell.edu; Sarah.Kang@mpimet.mpg.de

https://doi.org/10.1038/s41561-025-01669-5

SST and regional precipitation responses. When CO_2 concentration is abruptly quadrupled in climate models, the eastern equatorial Pacific warming is initially muted but gradually evolves to an El Niño-like warming pattern[12] (Extended Data Fig. 1d). The regional precipitation over East Asia and the western United States also slowly increases following the slow timescale of the El Niño-like warming[13] (Extended Data Fig. 1e,f). Notably, the slowly emerging processes are the primary contributors to the multi-model mean and inter-model spread of the long-term responses (Extended Data Fig. 1g–i). This raises a critical question: what process in the slow timescale governs the uncertainty of the tropical Pacific warming and, consequently, the regional precipitation enhancements?

Building on these insights, we hypothesize that delayed warming of the Southern Ocean (SO) is a key slow process. Initially, ocean circulation over the SO mitigates SST warming by absorbing heat into the deep ocean. This ocean heat uptake gradually slows, and manifests as the delayed SO warming[14]. Meanwhile, the anomalous SO warming causes the tropical Pacific to warm, particularly in the eastern basin, inducing the El Niño-like warming pattern, as revealed by recent idealized model experiments[15–17]. In this Article, through a series of climate model experiments, we demonstrate that tropical ocean warming, including with an El Niño-like pattern, is partly attributable to the delayed SO warming. This SO warming, in turn, increases precipitation during summer in East Asia and winter in the western United States, through teleconnections from the tropical SST changes. We show that Southern Hemisphere low cloud feedback modulates the entire teleconnection from the SO, partially explaining the inter-model spread of the regional precipitation projections over East Asia and the western Unites States.

Tropical ocean warming linked to the delayed SO warming

The teleconnection from the delayed SO warming emerges in the slow response. In this study, we define the slow response as the difference between the last and first 30 years of the 150-year CMIP6 abrupt-4xCO2 simulation, in which CO_2 is abruptly quadrupled from pre-industrial levels[18] (Methods). In this section we will focus on the remote impact the delayed SO warming has on the tropical SSTs, before investigating the impact on regional precipitation.

With abrupt CO_2 increases, the SO initially absorbs heat from the atmosphere, but gradually releases it around 45° S (Fig. 1a). Consequently, in the CMIP6 slow response, the SST warming is pronounced between 60° S and 40° S, indicating delayed SO warming (Fig. 1b). Meanwhile, the tropical Pacific warms in a triangular shape from the South Pacific (Fig. 1b, purple triangle), corresponding to El Niño-like warming (Supplementary Fig. 1). To isolate the effect of the delayed SO warming, we conducted a numerical experiment with the CESM1-CAM4 fully coupled model, wherein a regional thermal forcing is applied between 40° S and 60° S (Methods). The prescribed SO heating induces a response that resembles the CMIP6 slow response (compare Fig. 1c and 1b), with a high pattern correlation, 0.76 over the tropical Pacific between 30° S and 30° N and 120° E and 300° E. In other words, an anomalous zonally uniform heating to the SO drives global-scale teleconnections, including a warming of the eastern Pacific. Therefore, the delayed SO warming partially contributes to the tropical Pacific SST pattern of the slow response.

Previous studies have revealed the physical mechanisms by which zonally uniform SO heating induces El Niño-like warming over the tropical Pacific[15,16,19–21]. Specifically, SO warming is advected equatorward by the climatological southeasterlies west of South America[15]. The warm anomalies weaken these winds, leading to a reduction in evaporative cooling and coastal upwelling, which further amplifies the warming response[15,16,22]. The resulting Southeast Pacific SST warming reduces low cloud cover west of South America, and this positive low cloud feedback is the key that mediates the SO-driven teleconnection[15,16]. Once the warming reaches the eastern equatorial Pacific, the El Niño-like warming pattern is sustained by Bjerknes feedback.

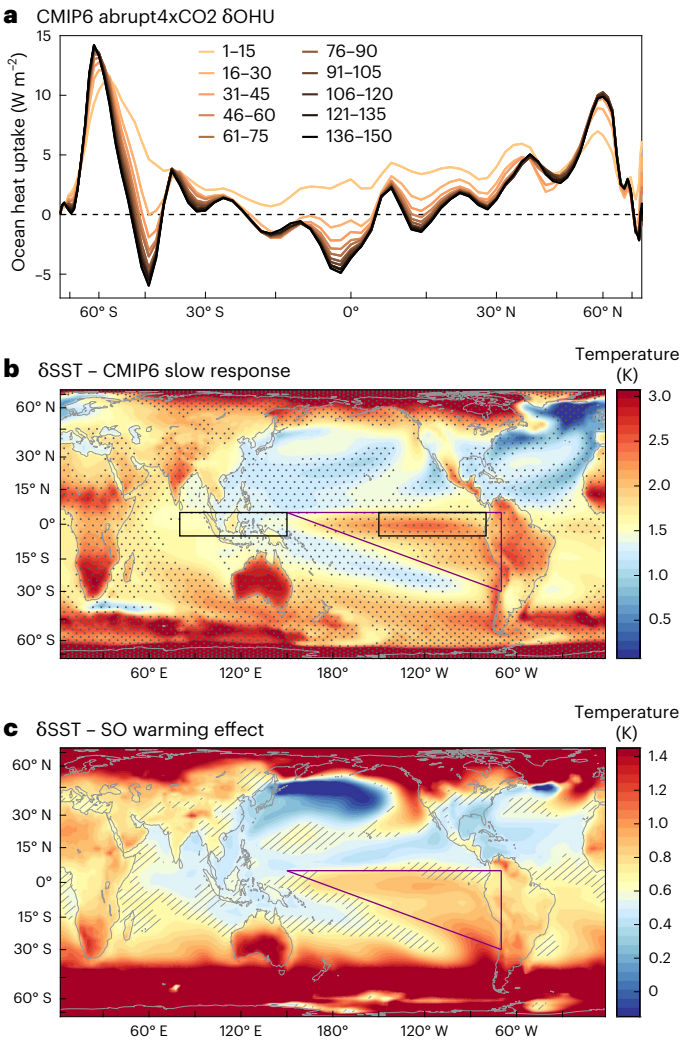


Fig. 1 | SO-to-tropics teleconnection. a, Muti-model and zonal mean ocean heat uptake (OHU) response of abrupt-4xCO2 relative to piControl, shown for 15-year periods. OHU corresponds to a downward positive net surface heat flux. **b**,**c**, Annual mean SST anomaly from the multi-model mean CMIP6 slow response to CO_2 quadrupling (**b**) and the CESM1-CAM4 SO warming experiment (**c**) (Methods). Note that the SST averaged over the tropics between 20° S and 20° N is used as the centre of the colour scale to emphasize the tropical SST pattern. Stippling in **b** indicates where >70% of 35 models agree on the sign of the pattern change. Unhatched shading in **c** indicates statistically significant signals at the 95% confidence using a *t*-test, compared to the inter-annual variability of the tropical SST pattern in the control climate.

The SO warming also propagates towards the tropical Indian Ocean and the tropical Atlantic Ocean (Fig. 1b,c). The west of Australia and South Africa exhibit climate states similar to those west of South America, with prevalent southeasterlies and stratocumulus clouds, thus exhibiting a similar teleconnection mechanism[15]. However, over the Indian Ocean, tropical warming is not evident in the SO warming experiment compared to the CMIP6 slow response. We suspect that this muted teleconnection towards the tropical Indian Ocean is due to the erroneously negative low cloud feedback west of Australia in CESM1-CAM4 (Supplementary Fig. 2 and Methods). Regardless of such tropical pattern differences, the delayed SO warming partially contributes to the enhanced equatorial warming—the stronger SST warming near the equator compared to the tropical ocean[7].

https://doi.org/10.1038/s41561-025-01669-5

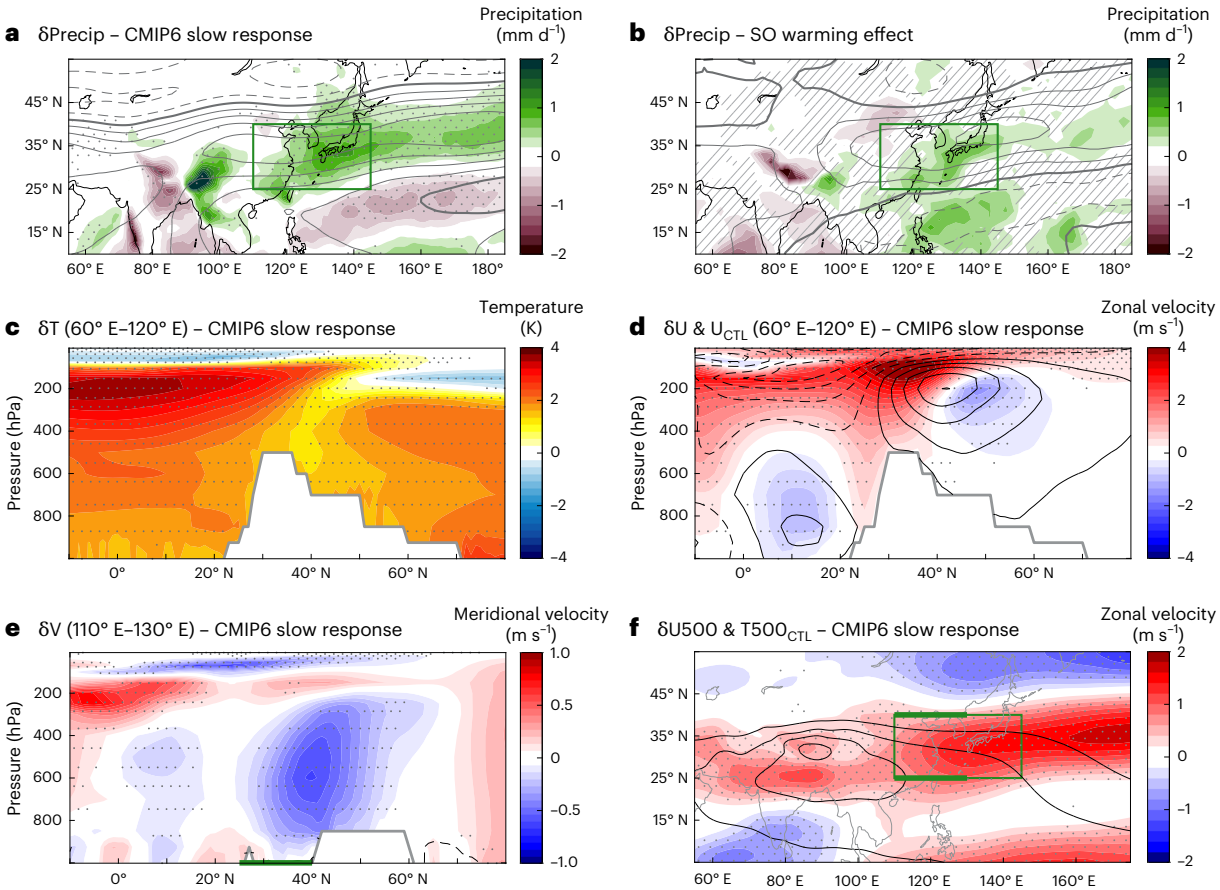


Fig. 2 | Remote impact on the East Asian summer (JJA) precipitation. **a**,**b**, Precipitation (shading) and 200-hPa zonal wind (contours) anomalies from the multi-model mean CMIP6 slow response (**a**) and the CESM1-CAM4 SO warming experiment (**b**). The solid (dashed) grey contours represent positive (negative) anomalies (interval = 0.8 m s^{-1}), where the thick line specifies zero. **c**–**f**, The multi-model mean CMIP6 slow response related to the southward Asian jet shift. **c**, Response in the vertical temperature profile averaged over the Asian sector (60° E–120° E). **d**, Response (shading) and climatology (contours; interval = 6 m s^{-1}) of the vertical profile of the zonal wind (U) over the Asian sector (60° E–120° E), with the solid (dashed) contours indicating westerly (easterly) winds. **e**, Vertical profile of the meridional wind (V) response (110° E–130° E). **f**, 500-hPa zonal wind changes (shading) and 500-hPa temperature climatology (contours; interval = 2 K from 265 K). The target East Asia domain is indicated by the green box in **a**, **b** and **f**, and the thick green line in **e** indicates the latitudes of the target East Asia domain. The thick green lines in **f** denote longitudes east of the Tibetan Plateau corresponding to **e**. Stippled and unhatched regions indicate statistical significance as in Fig. 1b,c. All variables are averaged for JJA.

The enhanced equatorial warming is dominantly shaped by the tropical Pacific heating (Fig. 1b,c and Supplementary Fig. 1).

Remote impact on East Asian precipitation

The delayed SO warming further contributes to the regional precipitation increases in the Northern Hemisphere, via tropical SST anomalies and subsequent atmospheric teleconnections. In this section we first focus on the precipitation over East Asia (25° N–40° N and 110° E–145° E) during the boreal summer months of June, July and August (JJA). This geographic domain includes a densely populated coastal region subject to flood risks, as well as portions of ocean, to capture the large-scale precipitation signal.

The East Asia summer precipitation increases in both the CMIP6 slow response and the response to the SO warming alone (Fig. 2a,b, green boxes). Thus, the slow increase in the East Asia summer precipitation can be partly attributed to the delayed SO warming. The atmospheric teleconnection occurring in the summer following El Niño in the winter illustrates the mechanism, which relies on enhanced equatorial warming increasing the East Asia summer precipitation by shifting the Asian jet southward[6–8,23].

First, the enhanced equatorial warming, driven by the delayed SO warming, leads to tropical upper-level warming following the moist adiabat (Fig. 2c). The resultant southward shift in the maximum meridional temperature gradient leads to the southward displacement of the Asian summer jet[23] (Fig. 2d). As the Asian jet shifts southward, the atmospheric column it passes through becomes shallower due to the elevated topography (Fig. 2d). Potential vorticity conservation implies a reduction in relative vorticity[24], and the subsequent anticyclonic flow triggered along the topography entails a northerly wind downstream of the Tibetan Plateau[8] (Fig. 2e). Northerly anomalies result in moisture convergence within East Asia and thereby lead to the precipitation increase[6]. In addition, the southward-shifted jet favours warm advection to East Asia in the mid-troposphere, as after the jet shift, the westerlies blow from the climatologically warmer regions over the Tibetan Plateau[25] (Fig. 2f). To balance the mid-tropospheric energy budget, the enhanced warm advection requires compensatory adiabatic cooling by anomalous upward motion (Supplementary Fig. 3). The anomalous upward motion enhances East Asia precipitation[26].

Indeed, the East Asia summer moistening is tightly linked to the southward jet shift across models, which is associated with the different degree of enhanced equatorial warming, hence the tropical Pacific warming (Extended Data Fig. 2 and Supplementary Fig. 1). The aforementioned dynamics in the CMIP6 slow response can be consistently identified in the SO warming experiment (compare Fig. 2c–f to Extended Data Fig. 3). In other words, the delayed SO warming causes the enhanced equatorial warming, shifting the Asian jet

https://doi.org/10.1038/s41561-025-01669-5

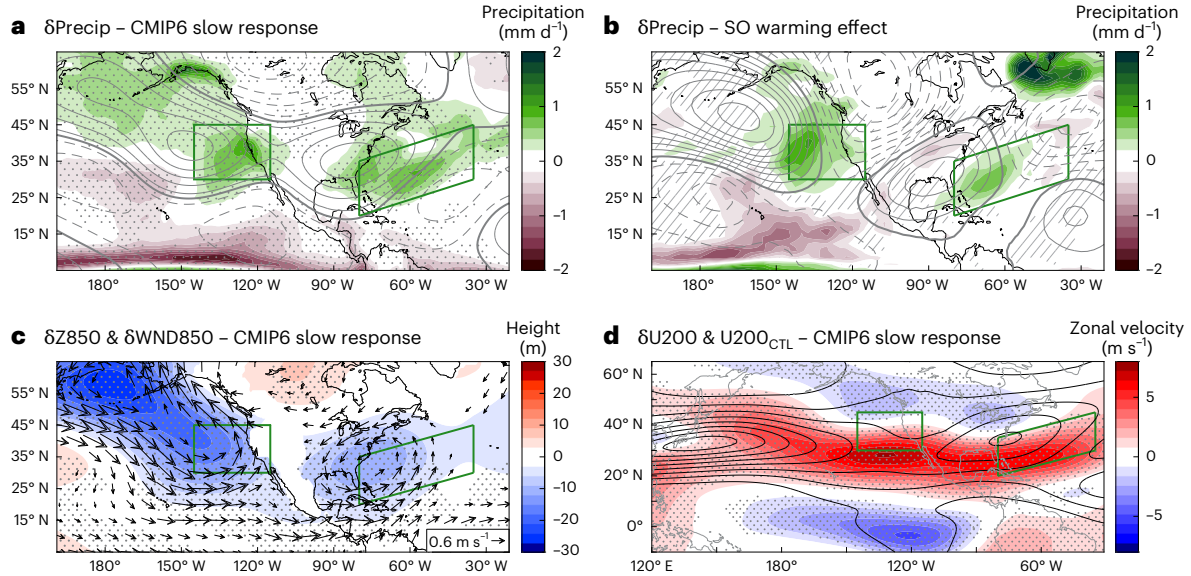


Fig. 3 | Remote impact on the United States winter (DJF) precipitation. **a**,**b**, Precipitation (shading) and 200-hPa geopotential height pattern (contours) anomalies from the multi-model mean CMIP6 slow response (**a**) and the CESM1-CAM4 SO warming experiment (**b**). The geopotential height pattern is calculated by subtracting the Northern Hemisphere average (0°–40° N) from the original value (Methods). The solid (dashed) grey contours represent negative (positive) anomalies (interval = 10 m). **c**,**d**, The multi-model mean CMIP6 slow response related to the Pacific/North America pattern. **c**, The 850-hPa geopotential height pattern (shading) and 850-hPa horizontal wind (vectors). The vectors are shown in the region where >70% of 35 models agree on the sign of either the zonal or meridional wind changes. **d**, The changes (shading) and climatology (contours) of the 200-hPa zonal wind. Only positive contours larger than 12 m s^{-1} are shown; the contour interval is 8 m s^{-1}. The green rectangle (parallelogram) corresponds to regions of western United States (southeastern United States) precipitation enhancement. Stippled and unhatched regions indicate statistical significance as in Fig. 1a,b. All variables are averaged for DJF.

southward, resulting in the anomalous northerly and mid-tropospheric warm advection east of the Tibetan Plateau, thereby increasing the East Asia precipitation.

Although dynamical mechanisms related to jet shift are consistent between the CMIP6 slow response and the SO warming experiment, the precipitation decreases south of East Asia only in the CMIP6 slow response (Fig. 2a,b). We attribute this difference to the muted warming over the tropical Indian Ocean in CESM1-CAM4 (Fig. 1b,c). In previous studies, the equatorial warming over the Indian Ocean relative to the western Pacific is shown to trigger a subtropical high-pressure anomaly over the western North Pacific[9,10]. The resulting anticyclonic flow enhances East Asia precipitation by supplying additional moisture, and the descent motion associated with the anticyclone decreases the precipitation south of the East Asia[9,27]. Indeed, the western North Pacific subtropical high-pressure anomaly is developed only in the CMIP6 slow response (Extended Data Fig. 4a,b). Similarly, the teleconnection mechanisms related to the subtropical high-pressure anomaly exist in the slow response but can be negligible in models in which the relative Indian Ocean warming is muted (Extended Data Fig. 4e–g).

Remote impact on precipitation around the United States

We now examine the slow CO_2-forced precipitation response in the western United States (30° N–45° N, 215° E–245° E) during the boreal winter months (December, January, February, DJF). Note that the selected region contains the highly populated coastal cities. The western United States precipitation increases in the CMIP6 slow response as well as in the SO warming experiment (Fig. 3a,b, green rectangles). Hence, the slow increase in the western United States winter precipitation is partly attributed to the delayed SO warming.

The wetting in the western United States can be induced by an El Niño-like teleconnection, starting from the delayed SO warming. Previous research has revealed that tropical Pacific warming induces low geopotential height anomalies reminiscent of the Pacific/North America (PNA) pattern via Rossby wave responses, thereby enhancing winter precipitation over the western United States[5,11]. Indeed, in response to the delayed SO warming, the 200-hPa geopotential height anomalies exhibit minima over the northeastern Pacific (Fig. 3a,b, grey contours), which resemble the responses in a typical El Niño year[28]. The resulting low height anomalies generate southwesterly winds directed towards the western United States (Fig. 3c), which in turn supply moisture and enhance precipitation. In addition, the low height anomalies in the northeastern Pacific correspond to the eastward extension of the Pacific jet, which would otherwise be concentrated in the western Pacific (Fig. 3d). Given that climatological storm track activity decreases from the Pacific to the western United States[29], this eastward jet extension steers more storms towards the western United States, thereby enhancing precipitation[30].

Accordingly, models with stronger tropical Pacific warmings tend to have lower height anomalies, modulating the western United States precipitation response among models (Extended Data Fig. 5a–c). In addition, the dynamic mechanisms behind the western United States moistening are similar in the CMIP6 slow response and the SO warming experiment (compare Fig. 3c,d to Extended Data Fig. 6a,b). Therefore, the delayed SO warming induces a tropical Pacific warming, triggering a low geopotential height anomaly over the northeastern Pacific, increasing moisture supply and steering more storms to the western United States, thereby intensifying precipitation there.

The slow precipitation increase in the southeastern United States is also partly explained by the SO-driven teleconnection. Precipitation during winter increases with the warming from the SO (Fig. 3a,b, green parallelograms). The tropical Pacific warming induces low height anomalies over the southeastern United States (Fig. 3a,b, grey contours), thereby increasing the rainfall in the southeastern United States as in El Niño years[31]. This El Niño-like teleconnection is further confirmed by the inter-model correlation between the tropical Pacific warming, low height anomaly and southeastern United States precipitation increase (Extended Data Fig. 5d–f).

https://doi.org/10.1038/s41561-025-01669-5

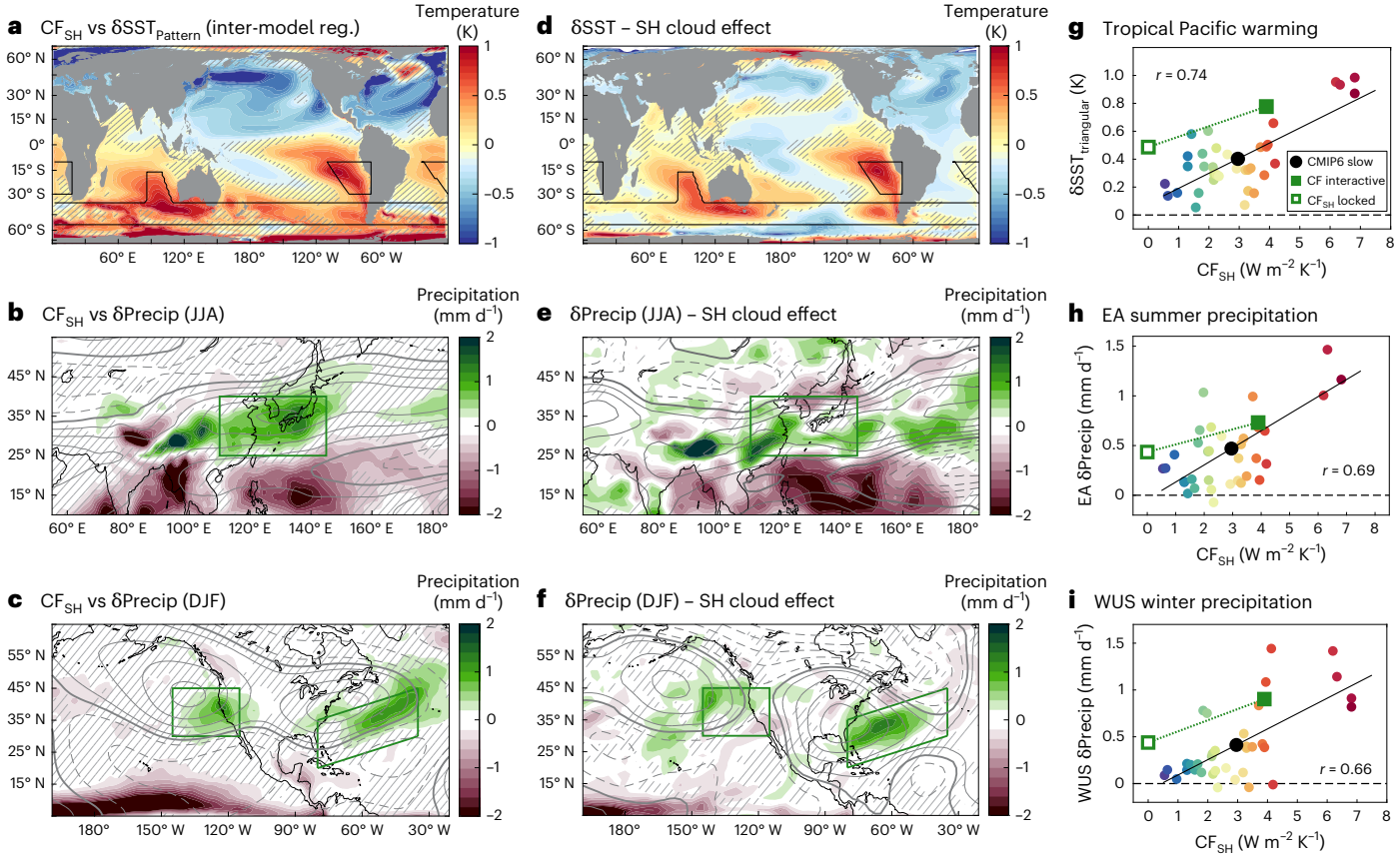


Fig. 4 | The Southern Hemisphere low cloud feedback as a key regulator of the teleconnection. a–c, Regression across models of the CMIP6 slow response onto CF_{SH} for the annual mean tropical SST pattern (**a**), precipitation (shading) and 200-hPa zonal wind (contours; interval = 0.8 m s^{-1}) during summer (JJA; **b**) and precipitation (shading) and 200-hPa geopotential height pattern (contours; interval = 10 m) during winter (DJF; **c**). **d–f**, Same variables as in **a–c** but for the CF_{SH}-induced responses estimated with regional cloud-locking experiments (Methods). Unhatched shading indicates statistically significant signals at the 95% confidence level using a *t*-test. **g–i**, CF_{SH} versus the CMIP6 slow responses for the tropical Pacific triangular warming (**g**); precipitation during the East Asian (EA) summer (**h**) and western United States (WUS) winter (**i**). Annotations indicate inter-model correlation coefficients. The symbols are colour-coded from blue to red in ascending order of the CF_{SH}. The black symbols indicate the multi-model mean, and open (filled) green rectangles indicate the CESM1-CAM5 experiment in which the clouds are regionally locked (globally interactive). In **i**, the western United States winter is defined as November, December, January for the CMIP6 slow response and as January, February, March for the cloud-locking experiment, when each signal is maximized.

Southern Hemisphere low cloud feedback as a key regulator

Likewise, the SO-driven teleconnections affect not only the tropical SSTs but also regional precipitation over East Asia, the western United States and the southeastern United States. Previous studies have identified Southern Hemisphere low cloud feedback as a key determinant of the teleconnection from the SO to the tropics[15,16]. Here we examine whether variations in low cloud feedback can explain the inter-model differences not only in tropical SST anomalies, but also in regional precipitation changes.

We first quantified the Southern Hemisphere low cloud feedback (CF_{SH}) as the sensitivity of the shortwave (SW) cloud radiative effect to underlying SSTs averaged over Southern Hemisphere regions with climatological low clouds[32], indicated by black boxes in Fig. 4a (Methods and Supplementary Fig. 4). We then regressed the CMIP6 slow response against CF_{SH} across different climate models (Fig. 4a–c). The models with a stronger CF_{SH} exhibit more warming in the SO and tropical oceans. To be specific, the triangular warming over the South Pacific becomes stronger, with a significant inter-model correlation of 0.74 (Fig. 4g). Furthermore, the models with a larger CF_{SH} tend to have a more pronounced increase in precipitation over East Asia and the western United States (Fig. 4b,c), with significant correlation coefficients (Fig. 4h,i). Therefore, the Southern Hemisphere low cloud feedback may amplify the SO-driven teleconnection, regulating the slow response of the tropical SST pattern as well as regional precipitation over the Northern Hemisphere.

We further quantified the role of CF_{SH} by means of a regional cloud-locking experiment. The abrupt-4xCO2 simulation with the default CESM1-CAM5 was compared with a simulation in which the cloud radiative feedbacks were disabled regionally over the climatological low cloud regions in the Southern Hemisphere (Methods and Supplementary Fig. 5). The differences in the slow response between the cloud-interactive and regional cloud-locked configurations represent the impact of CF_{SH} (Fig. 4d–f). The tropical Pacific warming and the regional precipitation increases were amplified with interactive CF_{SH} relative to the cloud-locked experiments (Fig. 4g–i, green rectangles). Therefore, it is evident that CF_{SH} regulates the global teleconnections from the SO in the models, as suggested by the similarity between the regional cloud-locking experiment and the inter-model regression map (Fig. 4a–f).

The atmospheric teleconnections discussed in previous sections propagate the uncertainty of the diverging CF_{SH} among models to regional precipitation change. For the East Asia precipitation increase, the southward jet shift and associated interaction with the Tibetan Plateau (Fig. 2c–f) explain the model uncertainty associated with CF_{SH}, shown by the consistent signals both in the inter-model regression

https://doi.org/10.1038/s41561-025-01669-5

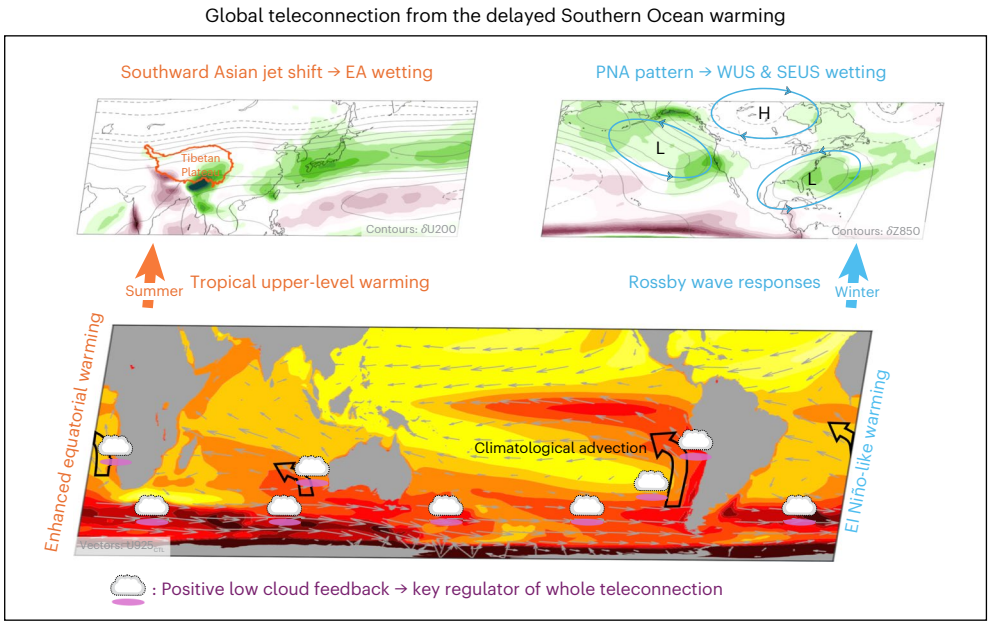


Fig. 5 | Schematic of the global teleconnection from the delayed SO warming. The delayed SO warming propagates equatorward, preferentially west of the continents, following the climatological southeasterlies. This equatorward teleconnection is further promoted by positive low cloud feedback. As the warming signal reaches the equator, it is further amplified by Bjerknes feedback, leading to the El Niño-like warming pattern. In summer, the enhanced equatorial warming heats the tropical troposphere following the moist adiabat, shifting the Asian jet southward and intensifying precipitation over East Asia (EA) due to strengthened interactions between the jet and the Tibetan Plateau. In winter, the El Niño-like warming induces the Rossby wave responses, producing a PNA circulation pattern with corresponding low (L) and high (H) pressure anomalies, which in turn enhances precipitation across the western United States (WUS) and southeastern United States (SEUS). The multi-model mean of the slow response in abrupt-4xCO2 and piControl climatology across the CMIP6 ensemble is used for the schematic.

(Extended Data Fig. 7) and the regional cloud-locking experiment (Extended Data Fig. 8). The stronger CF_{SH} also favours a stronger high-pressure anomaly over the western North Pacific subtropical regions (Extended Data Fig. 4c,d), explaining the reduced precipitation south of East Asia (Fig. 4b,e). For the western United States and southeastern United States precipitation enhancement, the Rossby wave responses and subsequent PNA pattern (Fig. 3c,d) are also amplified with a stronger CF_{SH} (Extended Data Fig. 6c–f).

Our analysis has concentrated on the slow climate response to abrupt CO_2 quadrupling, specifically the gradual evolution of tropical Pacific warming and related changes in regional precipitation. In fact, the Southern Hemisphere low cloud feedback explains the projection uncertainties not only for the slow responses, but also for the long-term responses (Extended Data Fig. 9). The inter-model correlation is dominated by four CESM2 variant models, but the cloud-locking experiment aligns with the inter-model relationship (compare the black regression lines and green dashed lines in Extended Data Fig. 9). Given that the cloud-locking experiment provides actual causal evidence, whereas the inter-model correlation does not, we argue that the CF_{SH} is partly responsible for the inter-model spread, even in the non-robust inter-model correlation. Thus, under the scenario with CO_2 enhancements, the misrepresentation of low clouds in the Southern Hemisphere will contribute to the projection uncertainties of tropical SSTs and regional precipitation changes over East Asia and the southeastern United States.

SO teleconnections to the Northern Hemisphere midlatitudes

Here we reveal a teleconnection in which the delayed SO warming expected under anthropogenic climate change contributes to enhanced equatorial warming with an El Niño-like pattern, thereby enhancing regional precipitation over East Asia, the western Unites States and the southeastern United States, as summarized in Fig. 5. The Southern Hemisphere low cloud feedback regulates the strength of the SO-driven teleconnection and partly explains the inter-model uncertainties of the regional precipitation projections. In fact, the highly model-dependent feedback from the Southern Hemisphere low clouds has been identified as a major source of uncertainty in global mean temperature increase and thus climate sensitivity[33,34]. Therefore, recent field campaigns focusing on the Southern Hemisphere low cloud[35,36] will prove valuable to improve not only climate sensitivity estimates but also regional precipitation projections.

In response to global warming, the slow teleconnections we describe here occur on centennial timescales as the SO slowly absorbs and releases heat, implying less impact on the near-future transient climate. However, the teleconnection impact will be more evident as humans reduce greenhouse gases (GHGs)—SO warming will persist while other regions will cool or equilibrate faster due to the differing heat capacities[37]. Indeed, in recent climate model experiments in which CO_2 is removed after transient quadrupling[38], SO warming becomes pronounced when CO_2 is removed (Fig. 6a–d). The SO warming sustains the enhanced warming over the tropical oceans, inducing dynamical changes identical to this study, thereby sustaining a precipitation increase over East Asia, the western United States and the southeastern United States (Fig. 6e–h). The sustained warming and wetting are consistent with recent studies with similar model experiments[27,39]. Eventually, long-term adaptation policies need to reflect these regional climate changes induced by SO warming, which will remain even with CO_2 reductions.

Generally, there is growing evidence indicating that the SO is a global climate pacemaker in recent trends, producing remote impacts such as those highlighted in this study[40–42]. Specifically, in the process of developing decadal climate predictions, higher spatial resolution has been shown to improve the prediction skill of surface temperature over the SO. This SO skill improvement extends to a better hindcast of the tropical Pacific SST as well as the western United States and

a Participating CMIP6 models

ACCESS-ESM1-5	CESM2
CNRM-ESM2-1	CanESM5
GFDL-ESM4	MIROC-ES2L
NorESM2-LM	UKESM1-0-LL

Target responses = yr[191–230] –yr[51–90]

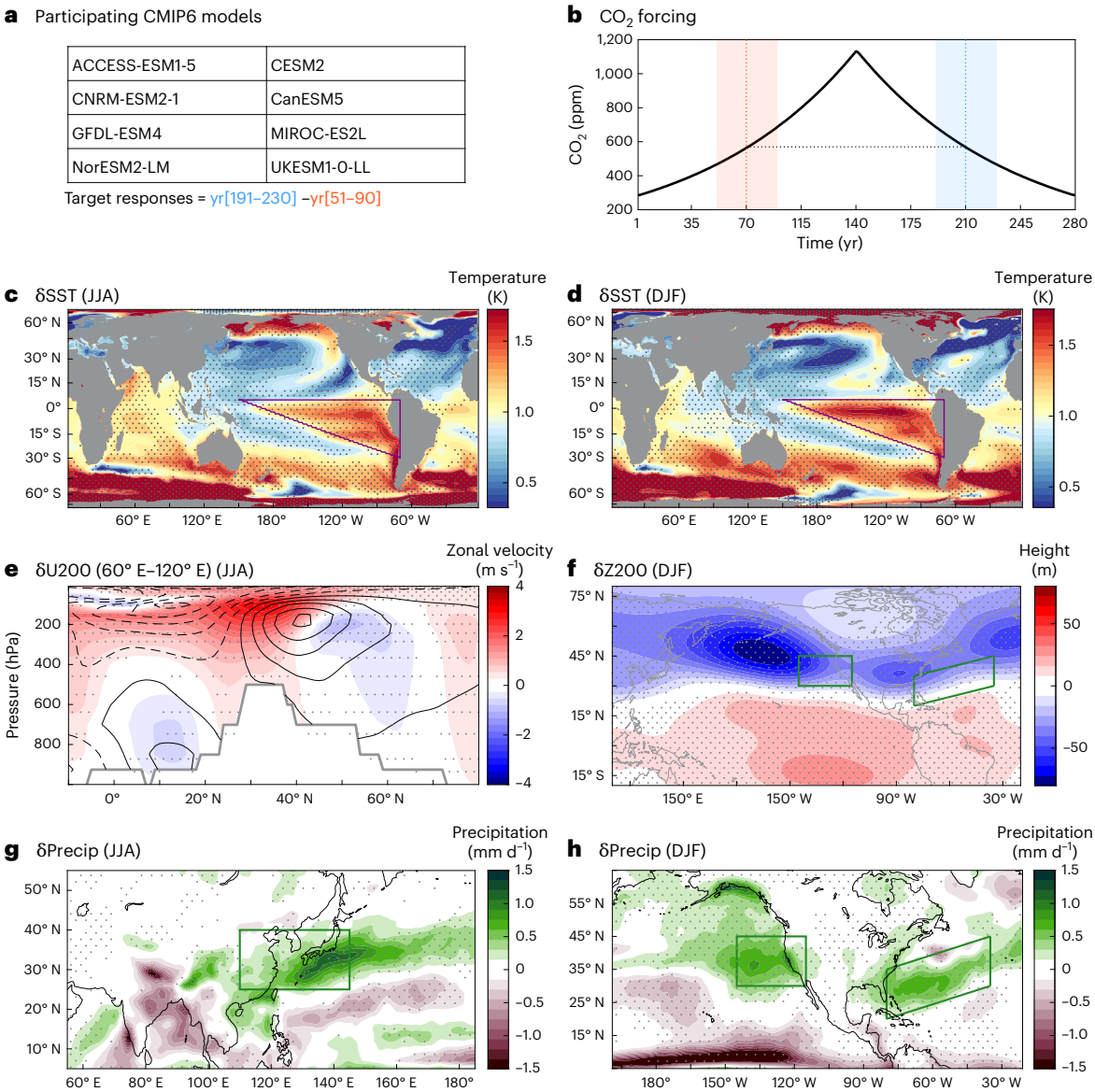


Fig. 6 | Long-term persistent climate changes related to the SO warming. **a**, Lists of CMIP6 models participating in the Carbon Dioxide Removal Model Intercomparison Project (CDRMIP)[38]. **b**, Transient CO_2 quadrupling and subsequent reduction used as the forcing in CDRMIP. The long-term persisting climate changes are measured by the difference between years 191–230 and 51–90 when CO_2 concentrations are identical. **c**,**d**, SST responses in summer (**c**) and winter (**d**). **e**, Vertical profile of zonal wind changes in summer (shading), with the corresponding climatology (contours; interval = 6 m s^{-1}). **f**, Responses in the 200-hPa geopotential height pattern during winter. **g**,**h**, Precipitation responses in summer (**g**) and winter (**h**). Stippling indicates where >6 of 8 models agree on the sign of the change. Green boxes are regions with precipitation enhancements investigated in this study.

southeastern United States precipitation during winter[42]. Therefore, an accurate representation of recent SO cooling trends may play a crucial role in resolving model–observation discrepancies of the recent tropical Pacific cooling as well as the western United States drying. The mechanisms revealed in this study lend further support to this hypothesis. These cumulative findings could help alleviate model errors in simulating recent regional precipitation trends and enable more trustworthy future projections.

Online content

Any methods, additional references, Nature Portfolio reporting summaries, source data, extended data, supplementary information, acknowledgements, peer review information; details of author contributions and competing interests; and statements of data and code availability are available at https://doi.org/10.1038/s41561-025-01669-5.

References

1. Zhang, W. et al. Increasing precipitation variability on daily-to-multiyear time scales in a warmer world. *Sci. Adv.* **7**, eabf8021 (2021).
2. Donatti, C. I. et al. Global hotspots of climate-related disasters. *Int. J. Disaster Risk Reduct.* **108**, 104488 (2024).
3. Howitt, R., MacEwan, D., Medellín-Azuara, J., Lund, J. & Sumner, D. *Economic Analysis of the 2015 Drought for California Agriculture* (UC Davis Center for Watershed Sciences, ERA Economics, UC Agricultural Issues Center, 2015).
4. Douville, H. et al. in *Climate Change 2021: The Physical Science Basis* (eds Masson-Delmotte, V. et al.) Ch. 8 (IPCC, Cambridge Univ. Press, 2023).
5. Allen, R. J. & Luptowitz, R. El Niño-like teleconnection increases California precipitation in response to warming. *Nat. Commun.* **8**, 16055 (2017).

6. Chiang, J. C. H., Fischer, J., Kong, W. & Herman, M. J. Intensification of the Pre-Meiyu Rainband in the Late 21st Century. *Geophys. Res. Lett.* **46**, 7536–7545 (2019).
7. Zhou, W., Xie, S.-P. & Yang, D. Enhanced equatorial warming causes deep-tropical contraction and subtropical monsoon shift. *Nat. Clim. Change* **9**, 834–839 (2019).
8. Kong, W. & Chiang, J. C. H. Southward shift of westerlies intensifies the East Asian early summer rainband following El Niño. *Geophys. Res. Lett.* **47**, e2020GL088631 (2020).
9. Xie, S.-P. et al. Indian Ocean capacitor effect on Indo-western Pacific climate during the summer following El Niño. *J. Clim.* **22**, 730–747 (2009).
10. He, C. & Zhou, T. Responses of the western North Pacific subtropical high to global warming under RCP4.5 and RCP8.5 scenarios projected by 33 CMIP5 models: the dominance of tropical Indian Ocean-tropical western Pacific SST gradient. *J. Clim.* **28**, 365–380 (2015).
11. Dong, L., Leung, L. R., Song, F. & Lu, J. Uncertainty in El Niño-like warming and California precipitation changes linked by the Interdecadal Pacific Oscillation. *Nat. Commun.* **12**, 6484 (2021).
12. Heede, U. K. & Fedorov, A. V. Eastern equatorial Pacific warming delayed by aerosols and thermostat response to CO_2 increase. *Nat. Clim. Change* **11**, 696–703 (2021).
13. Zappa, G., Ceppi, P. & Shepherd, T. G. Time-evolving sea-surface warming patterns modulate the climate change response of subtropical precipitation over land. *Proc. Natl Acad. Sci. USA* **117**, 4539–4545 (2020).
14. Armour, K. C., Marshall, J., Scott, J. R., Donohoe, A. & Newsom, E. R. Southern Ocean warming delayed by circumpolar upwelling and equatorward transport. *Nat. Geosci.* **9**, 549–554 (2016).
15. Kim, H., Kang, S. M., Kay, J. E. & Xie, S.-P. Subtropical clouds key to Southern Ocean teleconnections to the tropical Pacific. *Proc. Natl Acad. Sci. USA* **119**, e2200514119 (2022).
16. Mechoso, C. R. et al. Can reducing the incoming energy flux over the Southern Ocean in a CGCM improve its simulation of tropical climate?: Southern Ocean-Tropics link in a CGCM. *Geophys. Res. Lett.* **43**, 11057–11063 (2016).
17. Xiang, B., Zhao, M., Ming, Y., Yu, W. & Kang, S. M. Contrasting impacts of radiative forcing in the Southern Ocean versus southern Tropics on ITCZ position and energy transport in one GFDL climate model. *J. Clim.* **31**, 5609–5628 (2018).
18. Eyring, V. et al. Overview of the Coupled Model Intercomparison Project Phase 6 (CMIP6) experimental design and organization. *Geosci. Model Dev.* **9**, 1937–1958 (2016).
19. England, M. R., Polvani, L. M., Sun, L. & Deser, C. Tropical climate responses to projected Arctic and Antarctic sea-ice loss. *Nat. Geosci.* **13**, 275–281 (2020).
20. Kang, S. M. et al. Walker circulation response to extratropical radiative forcing. *Sci. Adv.* **6**, eabd3021 (2020).
21. Shin, Y. et al. Evolution of the tropical response to periodic extratropical thermal forcing. *J. Clim.* **34**, 6335–6353 (2021).
22. Zhang, H., Clement, A. & Di Nezio, P. The South Pacific meridional mode: a mechanism for ENSO-like variability. *J. Clim.* **27**, 769–783 (2014).
23. Zhou, W., Leung, L. R. & Lu, J. Seasonally and regionally dependent shifts of the atmospheric westerly jets under global warming. *J. Clim.* **35**, 5433–5447 (2022).
24. Holton, J. R. *An Introduction to Dynamic Meteorology* (Elsevier, 2004).
25. Boos, W. R. & Kuang, Z. Dominant control of the South Asian monsoon by orographic insulation versus plateau heating. *Nature* **463**, 218–222 (2010).
26. Sampe, T. & Xie, S.-P. Large-scale dynamics of the Meiyu-Baiu Rainband: environmental forcing by the westerly jet. *J. Clim.* **23**, 113–134 (2010).
27. Song, S.-Y. et al. Asymmetrical response of summer rainfall in East Asia to CO_2 forcing. *Sci. Bull.* **67**, 213–222 (2022).
28. Horel, J. D. & Wallace, J. M. Planetary-scale atmospheric phenomena associated with the southern oscillation. *Mon. Weather Rev.* **109**, 813–829 (1981).
29. Chang, E. K. M., Zheng, C., Lanigan, P., Yau, A. M. W. & Neelin, J. D. Significant modulation of variability and projected change in California winter precipitation by extratropical cyclone activity. *Geophys. Res. Lett.* **42**, 5983–5991 (2015).
30. Neelin, J. D., Langenbrunner, B., Meyerson, J. E., Hall, A. & Berg, N. California winter precipitation change under global warming in the Coupled Model Intercomparison Project Phase 5 ensemble. *J. Clim.* **26**, 6238–6256 (2013).
31. Ropelewski, C. F. & Halpert, M. S. North American precipitation and temperature patterns associated with the El Niño/Southern Oscillation (ENSO). *Mon. Weather Rev.* **114**, 2352–2362 (1986).
32. Myers, T. A. et al. Observational constraints on low cloud feedback reduce uncertainty of climate sensitivity. *Nat. Clim. Change* **11**, 501–507 (2021).
33. Brient, F. & Schneider, T. Constraints on climate sensitivity from space-based measurements of low-cloud reflection. *J. Clim.* **29**, 5821–5835 (2016).
34. Tan, I., Storelvmo, T. & Zelinka, M. D. Observational constraints on mixed-phase clouds imply higher climate sensitivity. *Science* **352**, 224–227 (2016).
35. McFarquhar, G. M. et al. Observations of clouds, aerosols, precipitation, and surface radiation over the Southern Ocean: an overview of CAPRICORN, MARCUS, MICRE, and SOCRATES. *Bull. Am. Meteorol. Soc.* **102**, E894–E928 (2021).
36. Mechoso, C. R. et al. Ocean-cloud-atmosphere-land interactions in the southeastern Pacific: the VOCALS program. *Bull. Am. Meteorol. Soc.* **95**, 357–375 (2014).
37. Kim, S.-K. et al. Widespread irreversible changes in surface temperature and precipitation in response to CO_2 forcing. *Nat Clim. Change* **12**, 834–840 (2022).
38. Keller, D. P. et al. The Carbon Dioxide Removal Model Intercomparison Project (CDRMIP): rationale and experimental protocol for CMIP6. *Geosci. Model Dev.* **11**, 1133–1160 (2018).
39. Kug, J.-S. et al. Hysteresis of the intertropical convergence zone to CO_2 forcing. *Nat. Clim. Change* **12**, 47–53 (2022).
40. Kang, S. M., Ceppi, P., Yu, Y. & Kang, I.-S. Recent global climate feedback controlled by Southern Ocean cooling. *Nat. Geosci.* **16**, 775–780 (2023).
41. Kang, S. M. et al. Global impacts of recent Southern Ocean cooling. *Proc. Natl Acad. Sci. USA* **120**, e2300881120 (2023).
42. Yeager, S. G. et al. Reduced Southern Ocean warming enhances global skill and signal-to-noise in an eddy-resolving decadal prediction system. *NPJ Clim. Atmos. Sci* **6**, 107 (2023).

Publisher's note Springer Nature remains neutral with regard to jurisdictional claims in published maps and institutional affiliations.

Open Access This article is licensed under a Creative Commons Attribution-NonCommercial-NoDerivatives 4.0 International License, which permits any non-commercial use, sharing, distribution and reproduction in any medium or format, as long as you give appropriate credit to the original author(s) and the source, provide a link to the Creative Commons licence, and indicate if you modified the licensed material. You do not have permission under this licence to share adapted material derived from this article or parts of it.

The images or other third party material in this article are included in the article's Creative Commons licence, unless indicated otherwise in a credit line to the material. If material is not included in the article's Creative Commons licence and your intended use is not permitted by statutory regulation or exceeds the permitted use, you will need to obtain permission directly from the copyright holder. To view a copy of this licence, visit http://creativecommons.org/licenses/by-nc-nd/4.0/.

© The Author(s) 2025

Methods

CMIP analysis

We use monthly mean outputs of two fully coupled CMIP6[18] experiments: piControl and abrupt-4xCO2. piControl mimics the climate with a pre-industrial CO_2 concentration (280 ppm), and abrupt-4xCO2 simulates the climate with quadrupled CO_2. We calculated the total response to CO_2 quadrupling as the difference between the last 30 years of abrupt-4xCO2 and the last 100 years of piControl. We calculated the slow response as the last minus first 30 years of abrupt-4xCO2, in which the effects of ocean dynamics and slowly evolving SSTs dominate. Although previous studies used the first ten years to capture the slow evolution of the SST, here we use the first 30 years to minimize the high internal variability in regional precipitation. This definition of the slow response clearly characterizes the delayed SO warming and associated global impacts (Supplementary Fig. 6). All CMIP6 data are interpolated to 1° × 1° horizontal resolution, and one ensemble per model was used for the analysis. A total of 35 models were selected based on their data availability (model lists are provided in Supplementary Table 1).

The SO warming experiment using CESM1-CAM4

To confirm the SO-driven teleconnection impact, a SO warming experiment was conducted using the fully coupled CESM1-CAM4[43]. We first equilibrate to the pre-industrial climate and then added the SO warming to run a forced simulation for 150 years. The target warming was added to the longwave heat flux term in the ocean coupler code. We added a sinusoidal heat flux between 40° S and 60° S, with a maximum of 20 W m^{-2}. The averaged difference between the last 50 years of forced climate and last 100 years of pre-industrial climate was analysed. The imposed heat flux was eventually released towards the atmosphere (dashed–dotted blue line in Supplementary Fig. 6), affecting the global climate through teleconnections. Note that the tropical Pacific response in this experiment is weaker than in the CMIP6 slow response, even if the forcing magnitude is larger (Fig. 1b,c). The weaker response can be attributed to the weak positive low cloud feedback in CESM1-CAM4, which might dampen the cloud radiative anomalies and thus the teleconnection in this particular model (Supplementary Fig. 2). To be specific, the negative low cloud feedback west of Australia might hinder the equatorward propagation of the SO warming in CESM1-CAM4, muting the tropical Indian Ocean warming (Fig. 1c). Note that the SST response in the North Atlantic and North Pacific in the SO warming experiment differs from the CMIP6 slow response. In the SO warming experiment, the stronger North Atlantic warming and displacement of the North Pacific cooling maxima to the northwest modulate the jet streams, which could result in weaker precipitation signals over East Asia and the western United States. However, the overall teleconnection impacts from the tropical SST anomalies are consistent.

Estimating Southern Hemisphere low cloud feedback

In this study we aim to find the cause of the inter-model spread in the SW cloud radiative effect (SWCRE) responses over the Southern Hemisphere low cloud regions. We decompose the SWCRE response into the product of the forced SST response and the SWCRE sensitivity to SST, a relationship that holds, particularly for low cloud regions[33]. The SWCRE sensitivity at each grid point is the estimated strength of the local SW cloud feedback, which will be intrinsic to a model's parameterizations.

We calculated the local SW cloud feedback strength by regressing the monthly SWCRE at the top of atmosphere (TOA) onto the monthly SST at each model grid point, using the de-seasonalized and de-trended deviations of 100-year piControl simulations. The local SW cloud feedback was then averaged over the Southern Hemisphere low cloud regions, where the inter-model correlation between the SWCRE changes and the tropical Pacific triangular warming is large (Supplementary Fig. 4a,b, green and blue boxes). The averaged feedback is what we refer to as the Southern Hemisphere low cloud feedback (CF_{SH}). This low cloud feedback can explain the inter-model spread of SWCRE changes both in the subtropical and SO domains, even without considering SST changes (Supplementary Fig. 4d,e). This indicates that the difference in low cloud parameterization is the dominant cause of the inter-model spread in the SWCRE responses. We estimated the observational CF_{SH} with the same method, using the CERES-EBAF[44] for SWCRE and OISSTv5[45] for SST from March 2000 to February 2020.

Here, the Southern Hemisphere low cloud includes the cloud over the subtropics and SO, and the subtropical and SO cloud feedbacks are correlated among climate models ($r = 0.63$; Supplementary Fig. 4c). In addition, note that we directly link the low cloud and SWCRE changes to the SST. In previous studies using cloud-controlling factor analysis, estimated inversion strength is another important factor for explaining SWCRE changes[33,46,47]. However, for the Southern Hemisphere low cloud regions, the anticorrelation between the time series of SST and estimated inversion strength is strong, so the univariate regression with SST is sufficient to capture the inter-model spread of the SWCRE responses.

The CESM1-CAM5 regional cloud-locking experiment

To elucidate the role of CF_{SH}, we conducted regional cloud-locking experiments[48] using the fully coupled CESM1-CAM5[49]. First, the eight cloud parameters were extracted every 2 h from a randomly chosen year of the equilibrated pre-industrial simulation. Then, in the regional cloud-locking experiments, the 2-h cloud parameters were prescribed repetitively every year in the radiative transfer code for the target region. The target regions we focused on were the SO and off the west coast of all major Southern Hemisphere continents where CF_{SH} is defined. One abrupt-4xCO2 simulation was integrated for 150 years with the interactive clouds and locked clouds. The effect was that the SW cloud radiative forcing in the interactive cloud experiment was muted in the regionally locked experiment (Supplementary Fig. 5). The difference between the interactive and locked cloud experiments demonstrates the role of CF_{SH}. The slow response was used for the analysis as in CMIP. Note that the CESM1-CAM5 has relatively realistic SW cloud feedback strength over the SH low cloud regions when compared to other models (Supplementary Fig. 2d), confirming the fidelity of the cloud-locking experiment.

Tropical SST pattern and the geopotential height pattern

The tropical SST pattern was calculated as the SST from which the tropical (20° S–20° N) mean has been subtracted. For the 200-hPa and 850-hPa geopotential height patterns, the deviation from the Northern Hemisphere (0°–40° N) average value was used to capture the circulation responses under global warming, following a previous study[50].

Asian jet shift

The shift of the Asian summer jet was quantified as the change in meridional asymmetry of the 200-hPa zonal wind as follows. First, we took the 200-hPa zonal wind during the summer (JJA) over the Asian continent (60° E–120° E). Next, we calculated the climatological Asian jet position as the latitude of the maximum zonally averaged zonal wind. To assess the meridional asymmetry of the zonal wind (U200asy), the meridionally averaged zonal wind between the climatological jet position and 20° south of the jet was subtracted from that between the climatological jet and 20° north of the jet. Negative changes in $U200_{asy}$ denote a southward shift in the Asian summer jet.

Data availability

CMIP6 data are available from the ESGF data portals (https://esgf-node.llnl.gov/projects/esgf-llnl/). The post-processed CESM1-CAM4 Southern Ocean warming experiment and CESM1-CAM5 regional cloud-locking experiment are available at https://doi.org/10.5281/zenodo.14797112. The observational SST (OISST v2) can be downloaded

from the Physical Sciences Laboratory website (https://psl.noaa.gov/data/gridded/data.noaa.oisst.v2.html). The CERES-EBAF v4.1 TOA radiation data are available from https://ceres.larc.nasa.gov/data/. The post-processed data for reproducing figures are available at https://doi.org/10.5281/zenodo.14797112.

Code availability

The raw data were first averaged by NetCDF Operator (NCO; https://nco.sourceforge.net/). All calculations, analysis and visualizations were then carried out using MATLAB. The MATLAB codes are available at https://doi.org/10.5281/zenodo.14797112.

References

43. Gent, P. R. et al. The community climate system model version 4. *J. Clim.* **24**, 4973–4991 (2011).
44. Loeb, N. G. et al. Clouds and the Earth's Radiant Energy System (CERES) Energy Balanced and Filled (EBAF) Top-of-Atmosphere (TOA) Edition-4.0 Data Product. *J. Clim.* **31**, 895–918 (2018).
45. Reynolds, R. W., Rayner, N. A., Smith, T. M., Stokes, D. C. & Wang, W. An improved in situ and satellite SST analysis for climate. *J. Clim.* **15**, 1609–1625 (2002).
46. Qu, X., Hall, A., Klein, S. A. & Caldwell, P. M. On the spread of changes in marine low cloud cover in climate model simulations of the 21st century. *Clim. Dyn.* **42**, 2603–2626 (2014).
47. Ceppi, P. & Nowack, P. Observational evidence that cloud feedback amplifies global warming. *Proc. Natl Acad. Sci. USA* **118**, e2026290118 (2021).
48. Middlemas, E. A., Kay, J. E. & Medeiros, B. M. Quantifying the influence of cloud radiative feedbacks on Arctic surface warming using cloud locking in an Earth system model. *Geophys. Res. Lett.* **47**, e2020GL089207 (2020).
49. Hurrell, J. W. et al. The Community Earth System Model: a framework for collaborative research. *Bull. Am. Meteorol. Soc.* **94**, 1339–1360 (2013).
50. He, C. et al. Enhanced or weakened western North Pacific subtropical high under global warming? *Sci. Rep.* **5**, 16771 (2015).

Acknowledgements

H.K. and F.L. are supported by NOAA MAPP award no. NA21OAR4310349. H.K. and S.M.K. have been supported by the research programme for the carbon cycle between oceans, land and atmosphere of the National Research Foundation (NRF) funded by the Ministry of Science and ICT (NRF-2022M3I6A1090965). A.G.P. and F.L. acknowledge support from the US Department of Energy, Office of Science, Office of Biological and Environmental Research, Regional and Global Model Analysis (RGMA) component of the Earth and Environmental System Modeling Program under award no. DE-SC0022070 and National Science Foundation IA 1947282. P.C. is supported by UK Research and Innovation (UKRI) grants NE/V012045/1, NE/T006250/1 and EP/Y036123/1. The National Center for Atmospheric Research is sponsored by the National Science Foundation. We thank the developer of the Synda Transfer Module, which was used for downloading CMIP data (https://espri-mod.github.io/synda/index.html). S.-W.Y. is supported by the Korea Environment Industry and Technology Institute (KEITI) through Climate Change R&D Project for New Climate Regime funded by Korea Ministry of Environment (MOE) (2022003560001). Y.S. is supported by the National Research Foundation of Korea (NRF) grant funded by the Korea government (MSIT) (RS-2024-00334637). We deeply appreciate Y. Kamae and the other anonymous reviewers for their contributions to improving the paper.

Author contributions

H.K. and S.M.K. conceived the study and designed the experiments. H.K. carried out the analysis and wrote a first draft. H.K., Y.S. and S.-Y.S. performed modelling experiments. H.K., A.G.P. and F.L. analysed the teleconnection mechanisms in detail. All authors contributed to discussions of the results and revisions of the paper.

Competing interests

The authors declare no competing interests.

Additional information

Extended data is available for this paper at https://doi.org/10.1038/s41561-025-01669-5.

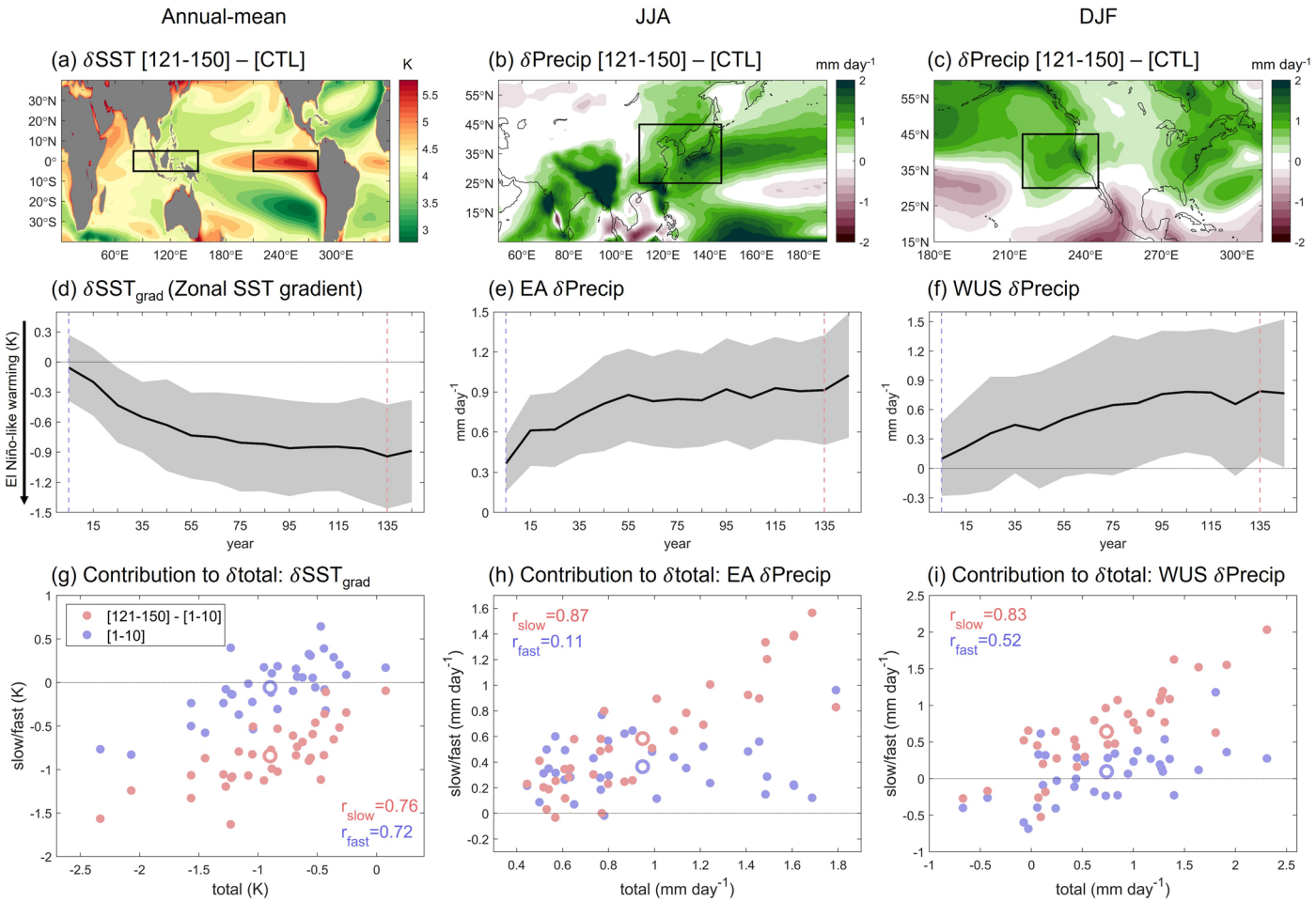
Supplementary information The online version contains supplementary material available at https://doi.org/10.1038/s41561-025-01669-5.

Correspondence and requests for materials should be addressed to Hanjun Kim or Sarah M. Kang.

Peer review information *Nature Geoscience* thanks Youichi Kamae and the other, anonymous, reviewers for their contribution to the peer review of this work. Primary Handling Editor: James Super, in collaboration with the *Nature Geoscience* team.

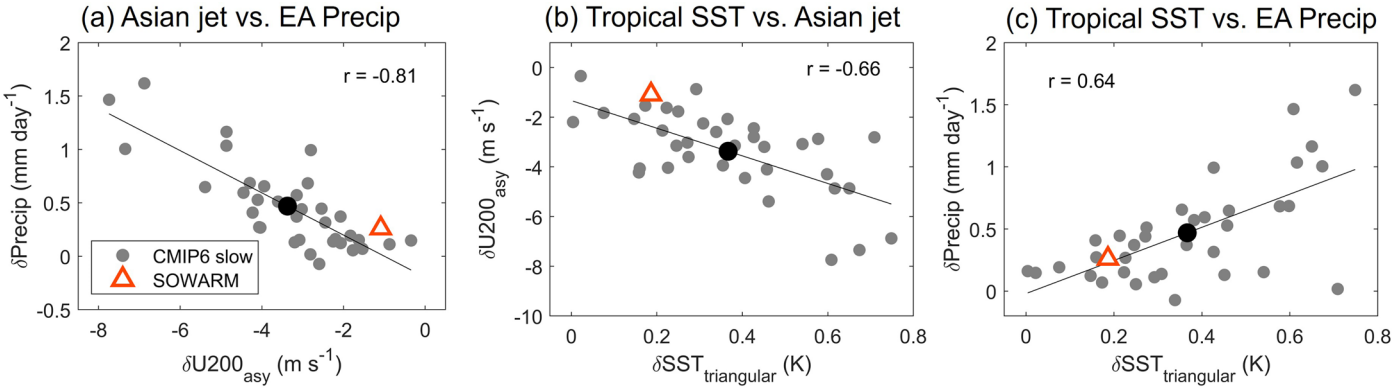
Reprints and permissions information is available at www.nature.com/reprints.

https://doi.org/10.1038/s41561-025-01669-5



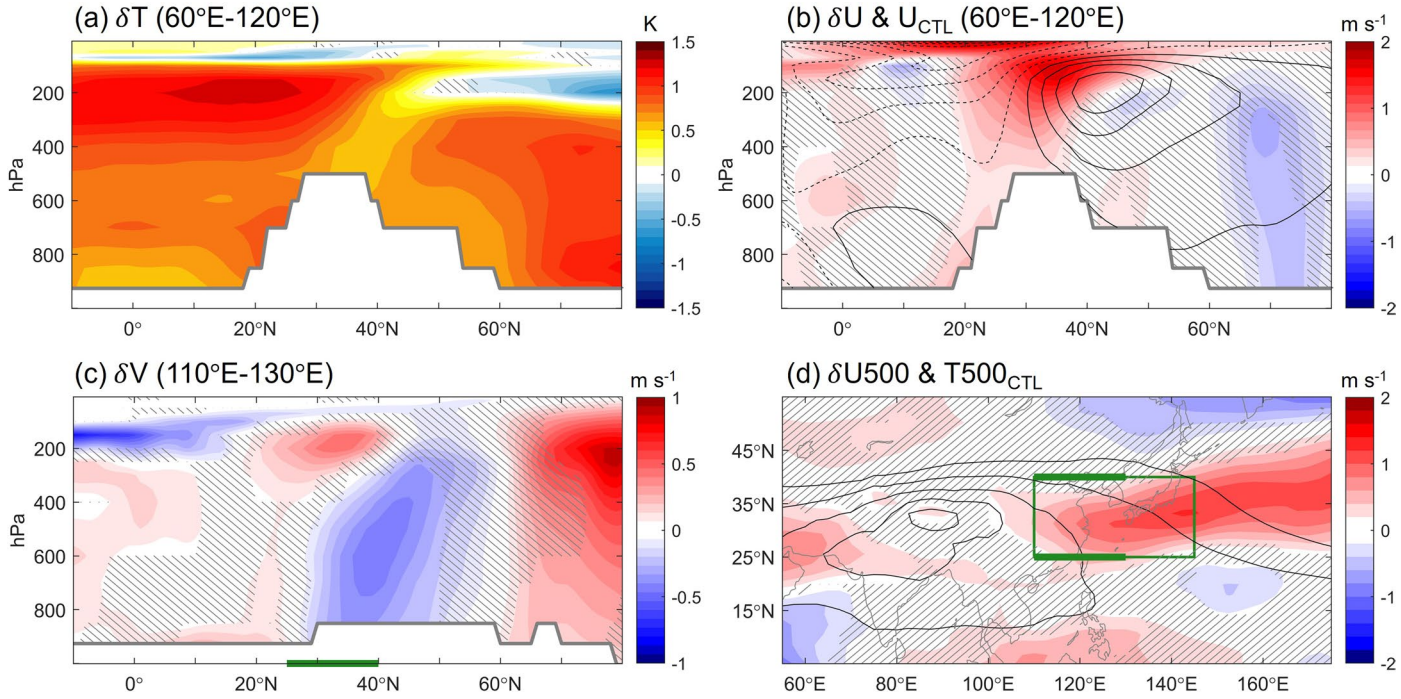
Extended Data Fig. 1 | Contribution of slow response to the total response in CMIP6 CO_2 quadrupling simulation. Total response is difference between last 30 years of abrupt-4xCO2 and last 100 years of pre-industrial control simulation, while slow response is difference between last 30 and first 10 years of abrupt-4xCO2 simulation. Fast response is subtraction of the slow from the total response. **a**–**c**, Multi-model mean total response in annual-mean SST (**a**), summer precipitation (**b**), and winter precipitation (**c**). **d**–**f**, Decadal averaged timeseries of the response in equatorial Pacific SST gradient (**d**), precipitation over East Asia (**e**) and the Western United States (**f**). The zonal SST gradient and regional precipitations are calculated over the black boxes in (a-c). Black lines represent multi-model mean and shading indicate ±1 inter-model standard deviation. **g**–**i**, Total responses versus slow/fast responses for equatorial Pacific SST gradient (**g**), precipitation over East Asia (**h**) and the Western United States (**i**). Red (Blue) circles indicate the slow (fast) responses, and the open circles indicate the multi-model mean. For slow/fast response, inter-model correlation coefficients to the total response are inserted as text. Note that the definition of slow response—which uses first 10 years—is specific to this figure; in main analysis we use first 30 years to minimize the internal variability of the regional precipitation (Methods).

https://doi.org/10.1038/s41561-025-01669-5



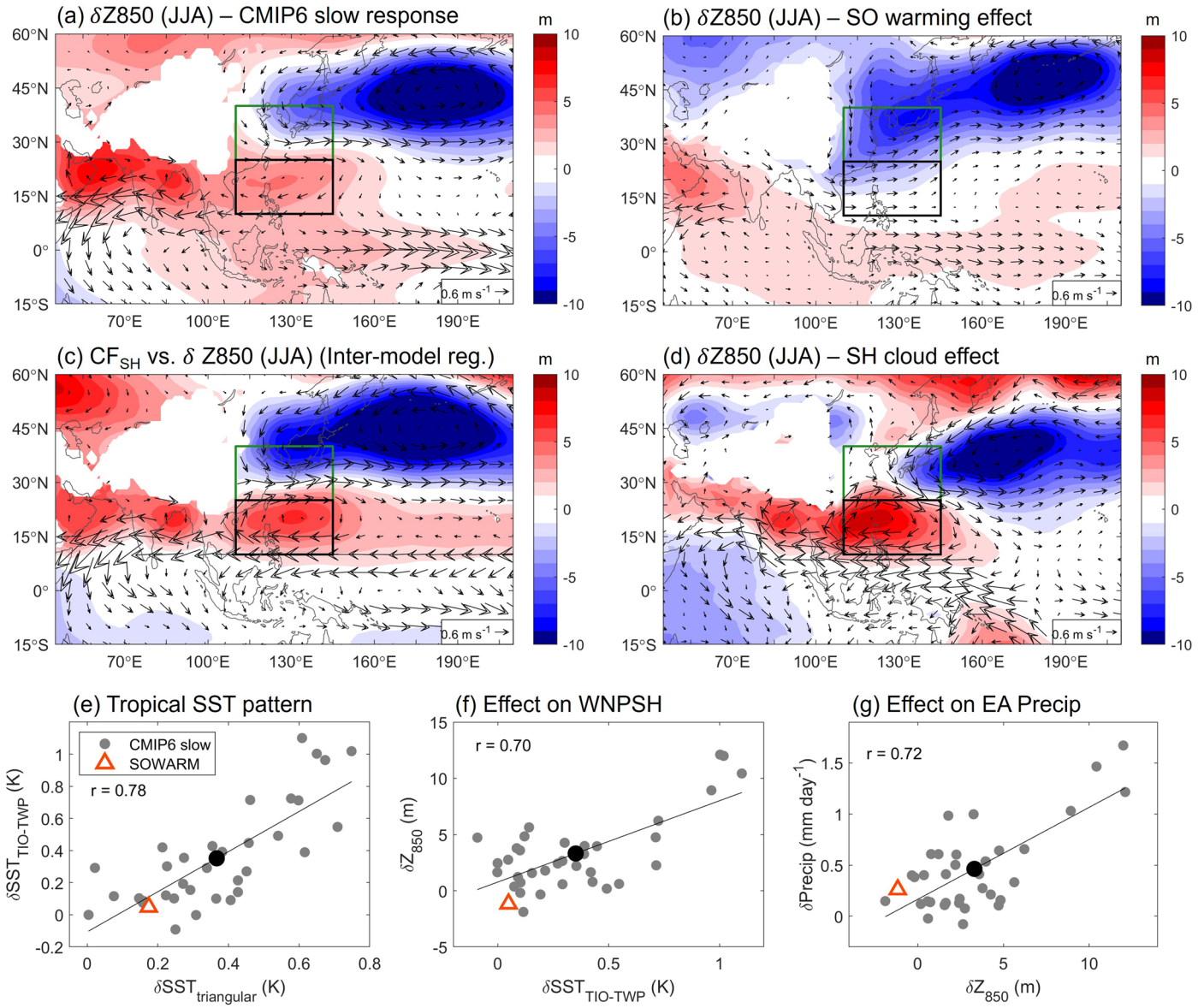
Extended Data Fig. 2 | The impact of the tropical SST anomalies and the Asian jet shift on the East Asian summer (JJA) precipitation. a–c, Relationship between the Asian jet shift and the East Asian (EA) precipitation changes (**a**), the tropical Pacific triangular warming and the Asian jet shift (**b**), and the triangular warming and the EA precipitation changes (**c**). The Asian jet shift is measured by changes in meridional asymmetry of 200-hPa zonal wind, in which negative sign indicates southward shift (Methods). The precipitation anomaly is averaged over EA between 25°N-40°N and 110°E-145°E (green boxes in Fig. 2a,b). Circle symbols are CMIP6 slow responses, black is multi-model mean. Orange triangles indicate the CESM1-CAM4 SO warming experiment. The inter-model correlation coefficients are inserted as text. All variables are averaged for JJA.

https://doi.org/10.1038/s41561-025-01669-5



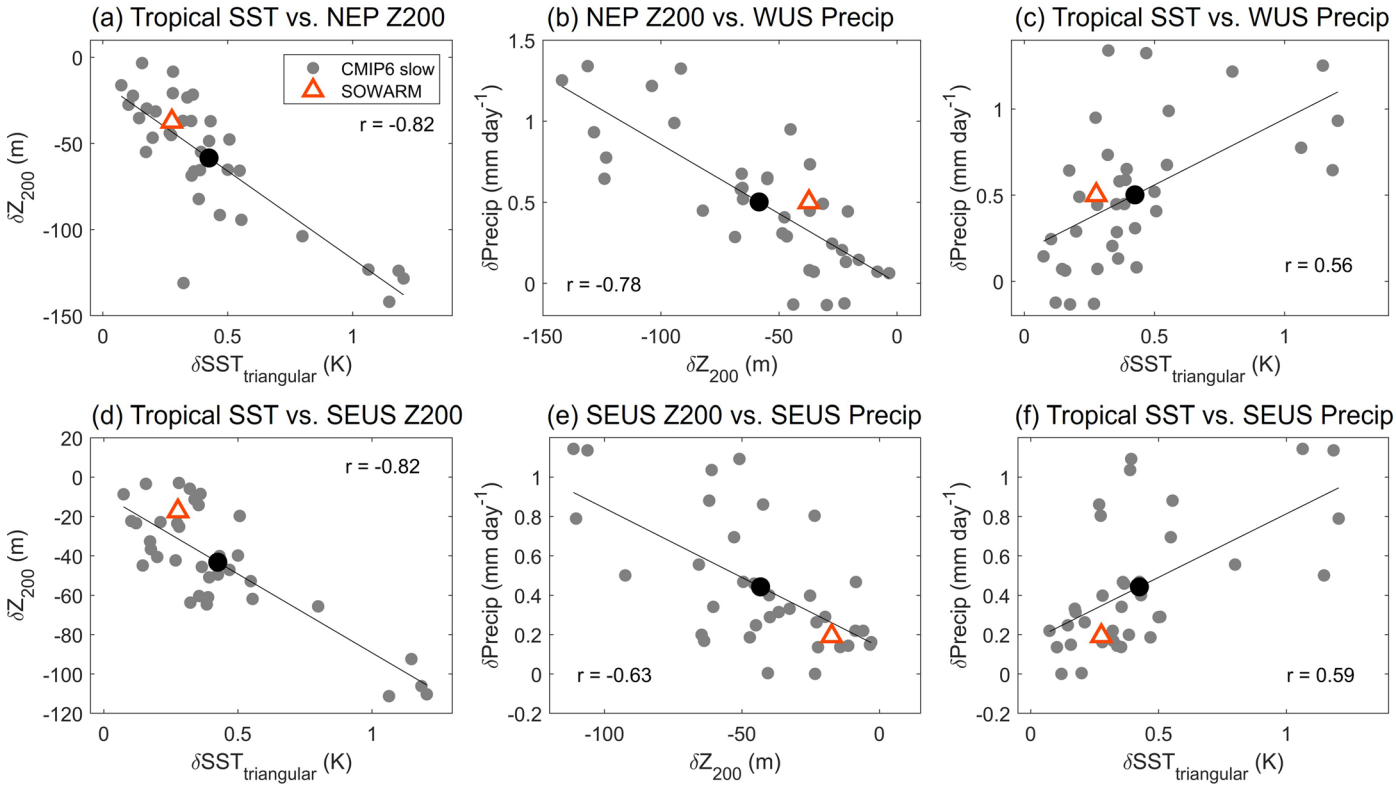
Extended Data Fig. 3 | The atmospheric teleconnection from the tropics to East Asia in the SO warming experiment. a–d, Same to Fig. 2c–f but for the CESM1-CAM4 SO warming experiment. Unhatched regions indicate statistically significant responses at the 95% confidence level using a *t* test, compared to the inter-annual variability in control climate.

https://doi.org/10.1038/s41561-025-01669-5



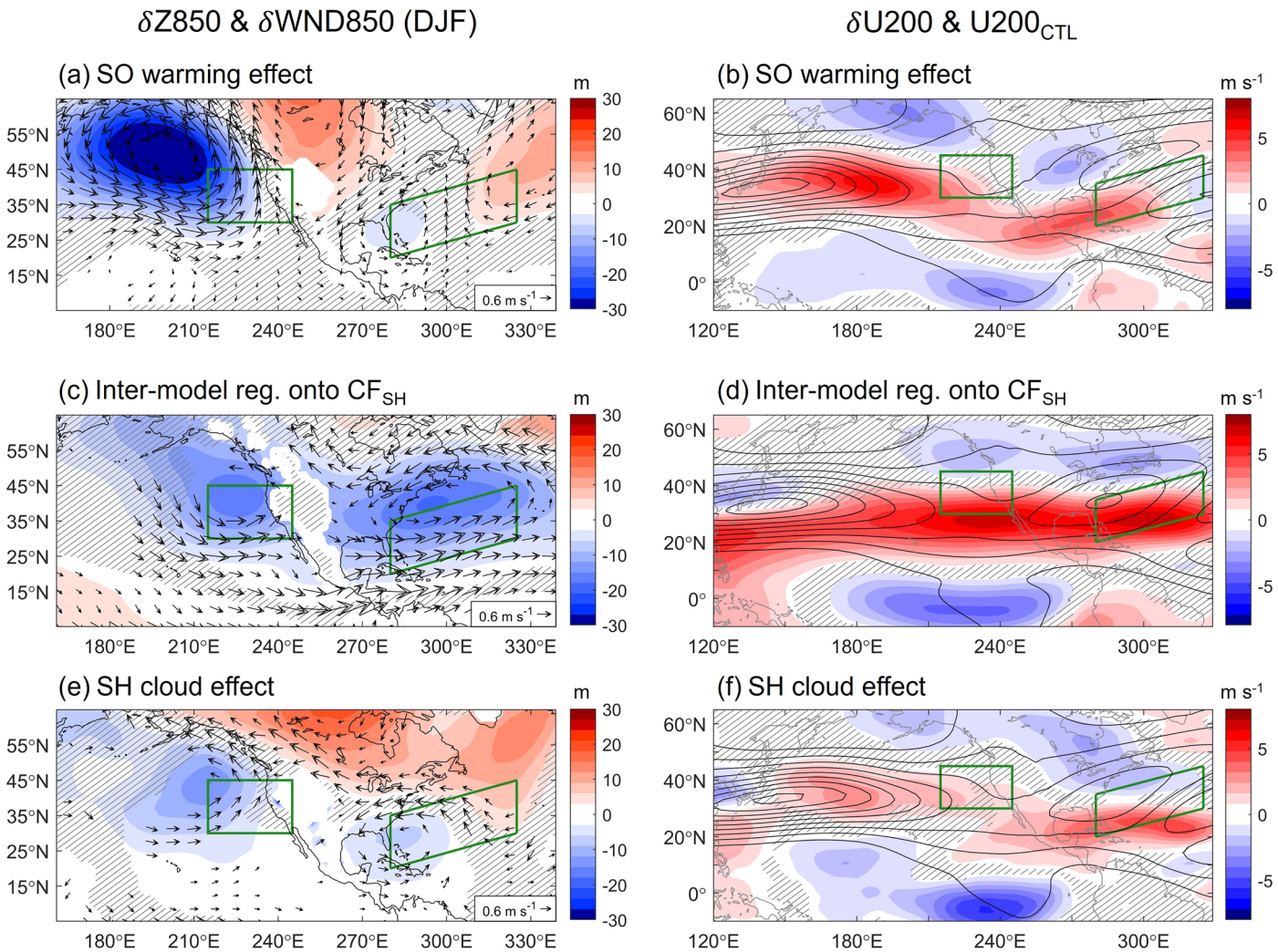
Extended Data Fig. 4 | The western North Pacific subtropical high linked to the tropical SST anomalies during summer (JJA). a–d, 850-hPa geopotential height pattern (shading) and 850-hPa horizontal wind (vectors) from multi-model mean CMIP6 slow response (**a**), CESM1-CAM4 SO warming experiment (**b**), inter-model regression of CMIP6 slow response onto the CF_{SH} (**c**), and CESM1-CAM5 regional cloud-locking experiment (**d**). **e-g**, Relationship between the tropical Pacific triangular warming and the relative warming over the tropical Indian ocean between 10°S-10°N and 50°E-100°E, compared to the tropical western Pacific between 10°S-10°N and 150°E-180°E (**e**), the relative tropical Indian ocean warming and the western North Pacific subtropical high (WNPSH) height anomaly (**f**), the height anomaly and the East Asia summer precipitation enhancement (**g**). The WNPSH height anomaly is calculated as the averaged 850-hPa geopotential height pattern (Methods) over the western North Pacific between 10°N-25°N and 110°E-145°E (black boxes in (a-d)). Annotations in (e-g) follow those in Extended Data Fig. 2. All variables are averaged for JJA.

https://doi.org/10.1038/s41561-025-01669-5



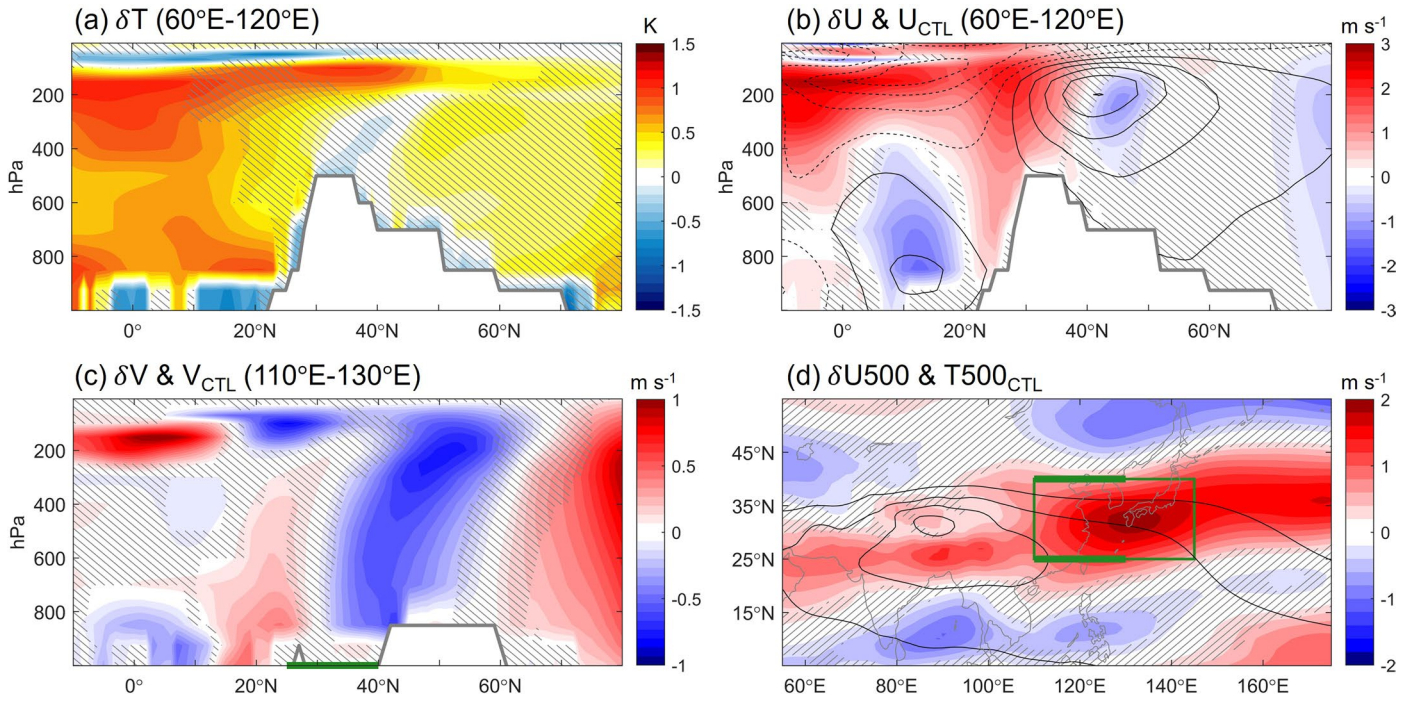
Extended Data Fig. 5 | The impact of the tropical SST anomalies and the Pacific/North America pattern on the precipitation around United States during winter (DJF). a–c, Relationship between the tropical Pacific triangular warming and the northeastern Pacific 200-hPa geopotential height pattern anomaly (**a**), the height anomaly and WUS precipitation enhancement (**b**), and the triangular warming and WUS precipitation enhancement (**c**). The height anomaly is averaged over the northeastern Pacific between 30°N–55°N and 185°E–235°E, and the precipitation anomaly is averaged over WUS between 30°N-45°N and 215°E-245°E (green boxes in Fig. 3a,b). **d–f**, Same relationship as in **a–c** except for the height anomalies over the southeastern United States (30°N–55°N and 185°E–235°E) and the SEUS precipitations averaged over the green parallelogram in Fig. 3a,b. The symbols and texts follow those in Extended Data Fig. 2. All variables are averaged for DJF.

https://doi.org/10.1038/s41561-025-01669-5



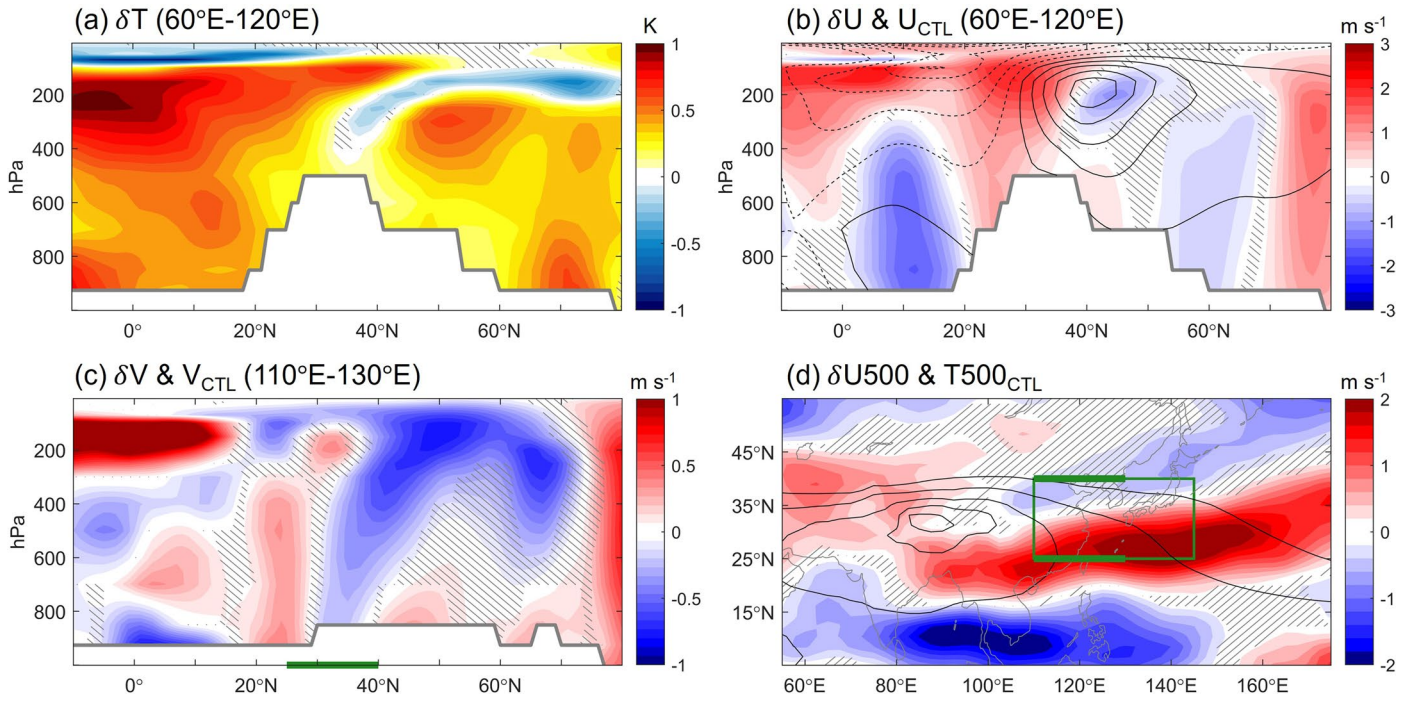
Extended Data Fig. 6 | The El Niño-like teleconnection to the Unites States. **a**,**c**,**e**, The 850-hPa geopotential height pattern (shading) and 850-hPa horizontal wind (vectors) from the CESM1-CAM4 SO warming experiment (**a**), the inter-model regression of CMIP6 slow response onto the CF_{SH} (**c**), and CESM1-CAM5 regional cloud-locking experiment (**e**). The vectors are shown if either the zonal or meridional component are statistically significant at the 95% confidence interval using a *t* test. **b**,**d**,**f**, Same as **a**, **c** and **e**, but for the changes (shading) and climatology (contours) of 200-hPa zonal wind. Only the positive contours larger than 12 m s^{-1} are shown; the contour interval is 8 m s^{-1}. Green boxes indicate the Western and Southeastern United States, where precipitation increases. All variables are averaged for DJF.

https://doi.org/10.1038/s41561-025-01669-5



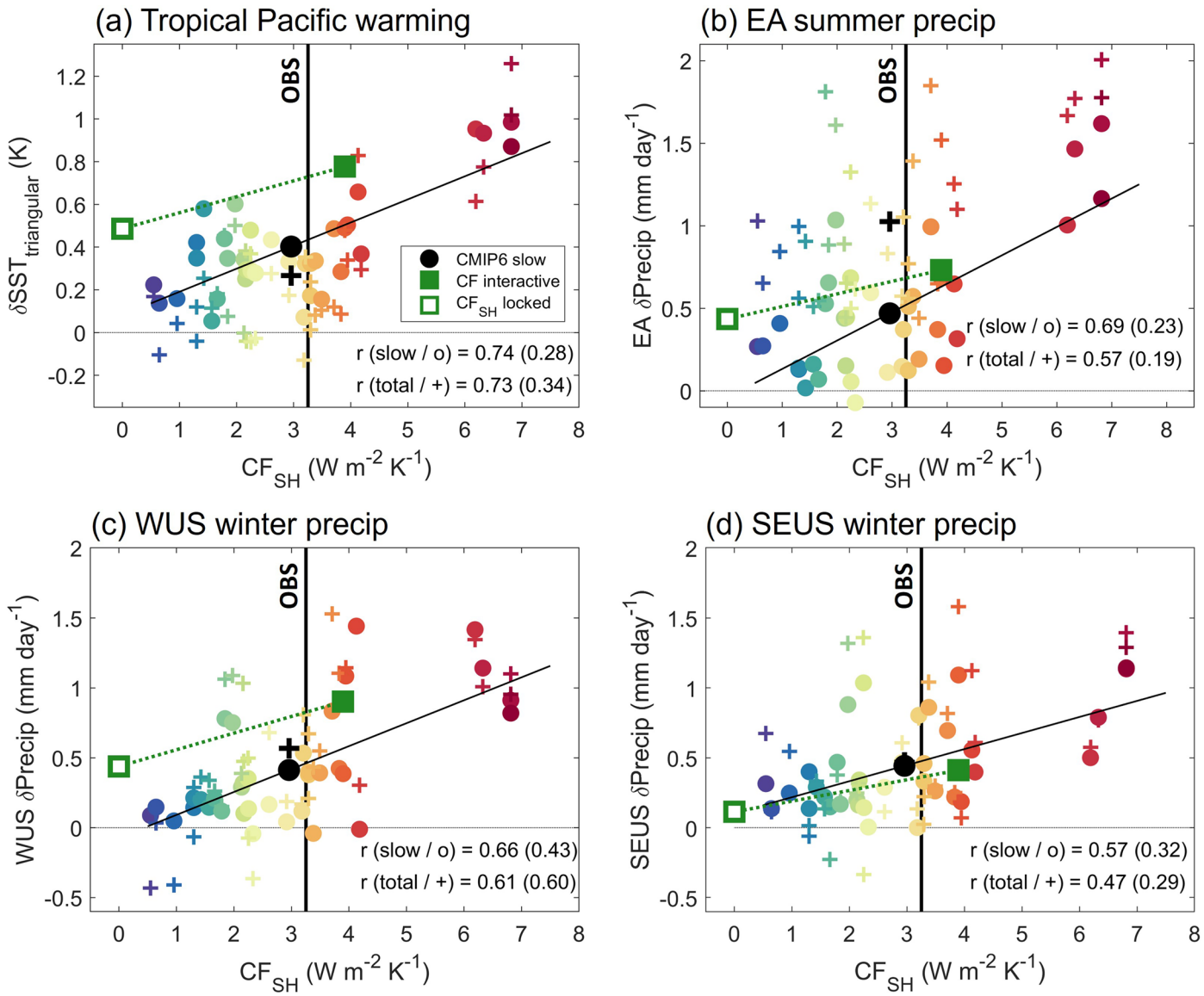
Extended Data Fig. 7 | The atmospheric teleconnection from the tropics to East Asia for the CMIP6 inter-model regression. a–d, Same to Fig. 2c–f but for the inter-model regression of CMIP6 slow response onto the CF_{SH}. Unhatched regions indicate statistically significant regression coefficients at the 95% confidence level using a *t* test.

https://doi.org/10.1038/s41561-025-01669-5



Extended Data Fig. 8 | The atmospheric teleconnection from the tropics to East Asia in the cloud-locking experiment. a–d, Same to Fig. 2c–f but for the CESM1-CAM5 regional cloud-locking experiment. Unhatched regions indicate statistically significant regression coefficients at the 95% confidence level using a *t* test.

https://doi.org/10.1038/s41561-025-01669-5



Extended Data Fig. 9 | The role of the Southern Hemisphere low cloud feedback (CF_{SH}) on the future projection uncertainties. a–d, CF_{SH} versus the tropical Pacific triangular warming (**a**), the precipitation responses during the EA summer (**b**), WUS winter (**c**), and SEUS winter (**d**). Circle (cross) symbols indicate CMIP6 slow (total) response. The inserted texts indicate inter-model correlation coefficients, where the values in parentheses are calculated after excluding four CESM2 variant models with the highest CF_{SH} (Supplementary Table 1). The symbols are color-coded from blue to red in ascending order of the CF_{SH}. Black symbol indicates muti-model mean and empty (filled) green rectangle indicates the CESM1-CAM5 experiment in which the clouds are regionally locked (globally interactive). The vertical black line indicates the observational estimate of CF_{SH} (Methods). Note that WUS winter is defined as November, December, January for CMIP6 slow response and as January, February, March for the cloud-locking experiment, when each signal is maximized.